

# Low computational cost semi-analytical magnetostatic model for magnetocaloric refrigeration systems

A. PLAÏT,<sup>1</sup> S. GIURGEA,<sup>1</sup> T. de LAROCHELAMBERT,<sup>1a)</sup> P. NIKA,<sup>1</sup> C. ESPANET<sup>1</sup>

<sup>1</sup>FEMTO-ST Institute, Univ. Bourgogne Franche-Comte, UTBM, CNRS,  
Energy Department, Parc Technologique, 2 av. Jean Moulin, F-90000 Belfort, France

**Abstract** - The analysis of the active magnetic refrigeration (AMR) cycle for different waveforms of both the magnetic field and the velocity of the heat transfer fluid is an essential challenge in designing and implementing heating and cooling systems based on the magnetocaloric effect. One of the most important issue is the correct modelling of the magnetic and thermal behavior of the active magnetocaloric materials (MCM) in order to estimate precisely cooling capacity of the magnetocaloric system. As the multiphysics coupling implies successive calls for both the thermal and the magnetic modelling subroutines, the execution time of these subroutines has to be as short as possible.

For this purpose, a new magnetostatic model based on reluctance network has been performed to calculate the internal magnetic field and the internal magnetic flux density of the active magnetocaloric material (gadolinium, Gd) inside the air gap of the magnetic circuit. Compared to a 3D Finite Element Model (FEM), our magnetostatic semi-analytical model leads to a sharp drop of the computation time, while offering a similar precision for all magnetic quantities in the whole magnetocaloric system.

*Keywords:*

Magnetocaloric refrigeration

Magnetocaloric regenerator

---

<sup>a)</sup> Author to whom correspondence should be addressed. Electronic mail: thierry.de-larochelambert@femto-st.fr

27 Magnetostatic model  
 28 Reluctance network  
 29 Magnetic equivalent circuit

30

31 **Nomenclature**

32	$I$	electrical current intensity, $A$	40	$U_m$	magnetomotive force, $A$
33	$H$	magnetic field, $A\ m^{-1}$	41	$N$	turn coil
34	$B$	magnetic flux density, $T$	42		
35	$T$	temperature, $K$	43	<i>Greek symbols</i>	
36	$R$	reluctance, $H^{-1}$	44	$\mu_0$	vacuum permeability, $H\ m^{-1}$
37	$L$	length, $m$	45	$\Phi$	magnetic flux, $Wb$
38	$S$	section, $m^2$	46	$\Theta$	magnetomotive force, $A$
39					

47 **1. Introduction**

48

49 The magnetic refrigeration and heat pumping is an emerging technology which offers  
 50 environmental benefits compared to conventional vapor compression machines.

51 The magnetic refrigeration is based on the magnetocaloric effect (MCE) exhibited by  
 52 some materials at room temperature.<sup>1</sup> The magnetocaloric effect occurs during the critical tran-  
 53 sition paramagnetic/ferromagnetic of these ferromagnetic materials: any change in external  
 54 magnetic field around the Curie temperature induces a reversible change in the correlated elec-  
 55 tronic spin entropy, directly related to strong specific thermal power density production/absorp-  
 56 tion. When these magnetization changes occur in an adiabatic way, they produce an adiabatic  
 57 temperature change  $\Delta T_{ad}$ , which is a characteristic property of the magnetic material and de-  
 58 pends on both the magnetic field evolution and the initial temperature. Since the best  $\Delta T_{ad}$  is in  
 59 the range of only a few kelvins per tesla, an active magnetic refrigeration (AMR) cycle has to  
 60 be imposed to magnetocaloric regenerators –micro-heat exchangers composed of magnetoca-  
 61 loric plates or spheres, etc.– to produce larger temperature gradients and significant thermal

62 power for heating or cooling purposes. An AMR cycle imposes a fluid (coolant) to flow alter-  
63 natively through the regenerator while synchronizing the magnetization-demagnetization of the  
64 regenerator.<sup>2</sup>

65 For several years, the Energy department of the FEMTO-ST Institute has been developing  
66 research on high efficiency magnetocaloric devices using magnetocaloric properties of some  
67 materials around ambient temperature.<sup>3</sup> This technology is meant to provide large-scale eco-  
68 logical solutions for refrigeration and heat pumping, since the theoretical efficiency of the AMR  
69 cycles is much higher than conventional vapor compression technologies. On the other hand,  
70 its operation does not require any use of greenhouse gases, unlike conventional refrigeration  
71 machines.

72 However, the design of such efficient magnetocaloric devices still requires further re-  
73 search for faster precise simulation codes and multiphysics models. This paper aims at exposing  
74 the theoretical basis and numerical results of a new model based on reluctance network applied  
75 to the Magnetic Equivalent Circuit of our magnetocaloric device, and showing the large im-  
76 provements provided in computational time for the simulation of large magnetocaloric systems,  
77 while offering a good compromise on its accuracy.

78

79 Even if models using reluctance network have been widely developed in electrical ma-  
80 chine modeling, there are very few reluctance network model in the magnetic refrigeration do-  
81 main.

82 Dai and al.<sup>4</sup> evaluate the influence of the gadolinium stack on the magnetic flux inside  
83 the air gaps of a magnetic circuit including permanent magnet, using an average permeability  
84 of the gap based on a simplified reluctance network, with an averaged magnetic flux density in  
85 the air gap. The magnetic field inside the gadolinium plates and the permeability of gadolinium  
86 are simply calculated by the means of the average field Brillouin function. The authors show  
87 that the change in temperature of the gadolinium stack strongly modifies the magnetic field in  
88 the gap, so that iso-field phases cannot be used for an accurate modeling of Ericsson cycles.  
89 However, nonlinear behavior of the ferromagnetic circuits is not considered.

90 More recently, Vuarnoz and al.<sup>5</sup> express the overall reluctance of the air gap as a series-  
91 parallel assembly of mean reluctances of the magnetocaloric plates, fluid layers and air gaps,  
92 allowing for the calculation of the mean magnetic flux and the corresponding magnetic flux  
93 density inside the plates. Using this model to calculate a simplified  $\Delta T_{ad}$ -based magnetocaloric  
94 heat-source term in a simple 1D thermo-fluidic model of an AMR cycle with imposed external

95 magnetic field, the authors find rather underpredicted values of the plates and fluid tempera-  
96 tures, however with less discrepancy compared to the results of simple uniform magnetic field  
97 models. Their calculations as well as their experimental results confirm the inability of perma-  
98 nent magnets to impose a constant internal magnetic field during cold or hot blows in AMR  
99 cycles, as shown previously in Ref. 4.

100 In this paper, a new magnetostatic model based on reluctance network is applied to the  
101 global magnetocaloric system in order to calculate the internal magnetic field and the internal  
102 magnetic flux density of the active magnetocaloric material (gadolinium, Gd). The model takes  
103 into account the non-linear behavior and non-homogeneity of the ferromagnetic materials,  
104 while highly reducing the computation time compared to a previous FEM model.

105

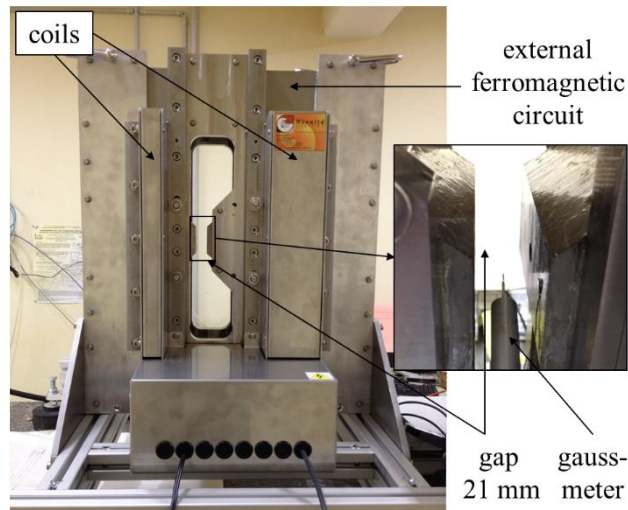
## 106 **2. Experimental prototype**

107

108 In the magnetic refrigeration domain, different prototypes based on active magnetic re-  
109 generative refrigeration (AMRR) principles were built and tested for more than twenty years.<sup>6</sup>

110 A specific experimental prototype has been developed and created in our laboratory (Fig.  
111 1), including a controlled power source for pulsed magnetic field (powerful electromagnet) and  
112 a controlled hydraulic cylinder specially designed to produce precise flow sequences through  
113 an active magnetocaloric regenerator block inserted between two micro-heat exchangers at both  
114 ends. The regenerator consists of 14 pure gadolinium rectangular parallel plates –12 central  
115 plates ( $13 \times 1 \times 45 \text{ mm}^3$ ) and 2 external plates ( $13 \times 0.5 \times 45 \text{ mm}^3$ ), all 0.5 mm apart from each  
116 other (Fig. 2) –; it is arranged inside the electromagnet 21 mm wide air-gap. The purpose of the  
117 bench is to characterize the thermofluidic behavior of the magnetocaloric regenerator and to  
118 optimize its refrigeration performances.<sup>7,8</sup>

119

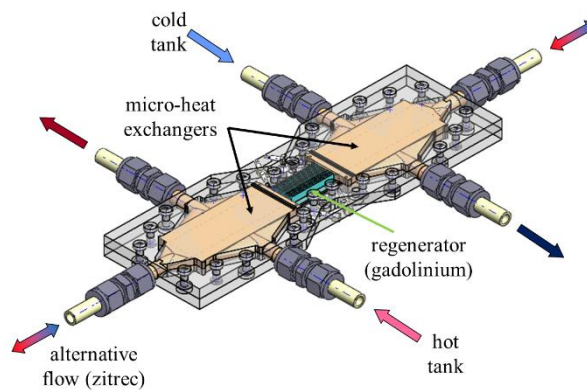


120

121

FIG. 1: *Femto-ST experimental prototype with gauss-meter to measure magnetic flux density*

122



123

124

FIG. 2: *Experimental magnetocaloric regenerator module*

125

### 126 **3. Magnetostatic modelling of the magnetocaloric system**

127

128

129

130

131

132

Many numerical models of AMR cycles have been developed in the last ten years. Among the most recent models, some consider the magnetic field equal to the applied field;<sup>9</sup> some others consider the magnetic flux density to be uniform in the whole material.<sup>10</sup> More precise models simply evaluate the internal magnetic field at each point of the regenerator by using averaged demagnetizing factors.<sup>11</sup>

133 In our previous work, a magnetostatic finite element model (FEM) was developed and  
134 implemented in a multiphysics analysis of the refrigeration test bench, and a significant mag-  
135 netic field heterogeneity was observed.<sup>12</sup> This heterogeneity can be explained by the strong  
136 dependence of the internal magnetization of the magnetocaloric material on the temperature  
137 close to its Curie point combined with the temperature gradient between cold and hot sides of  
138 the magnetocaloric regenerator. Another inhomogeneity factor is produced by 3D phenomena  
139 in the magnetic field distribution inside the air-gap of the magnetocaloric test bench.<sup>13</sup>

140 However, even if the magnetostatic FEM model offers a very accurate resolution of Max-  
141 well equations, its main drawback is the highly time-consuming calculation to solve these equa-  
142 tions in the whole magnetic domain. The computation time of the magnetostatic model is cru-  
143 cial, since it has to be used in each loop of the iterative calculation process until convergence  
144 of the multiphysics analysis, which requires a huge number of calls of the magnetostatic FEM  
145 model for each magnetocaloric operating point.<sup>8</sup>

146 In this work, a semi-analytical model is designed for both the magnetic flux density and  
147 the magnetic field calculation inside the whole magnetic system, allowing much faster calcula-  
148 tion than the FEM model with comparable precision, and accounting for the heterogeneous  
149 distribution of the magnetic field in the AMR cycle.

150 Since the main objective of our test bench is to precisely characterize the AMR cycle, it  
151 is important to estimate the magnitude of the magnetic field distribution inside the regenerator,  
152 accounting for the non-linear behavior of both the external magnetic circuit and the active mag-  
153 netic regenerator.<sup>14</sup>

154

### 155 **3.1. Magnetic device geometry and AMR discretization**

156

157 The electromagnet working was first simulated with FEM. The ferromagnetic circuit of  
158 the experimental prototype has an “8-shaped” structure presented in Fig. 3. It is composed of  
159 soft Fe-Si sheets, and a cylindric hole is arranged along the center line to enable further optical  
160 measurements of the fluid velocity (micro-PIV measurements). The pulse-controlled magnetic  
161 field is produced by 4 large coils with 90 turns each (colored rectangles on the side view, Fig.  
162 3).

163

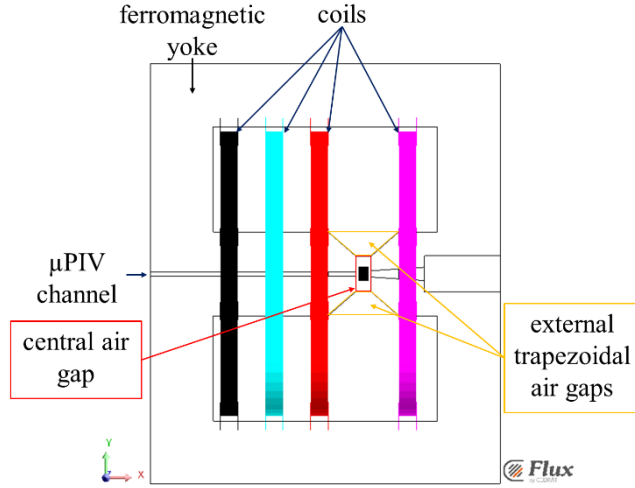


FIG. 3: *Electromagnet structure*

164

165

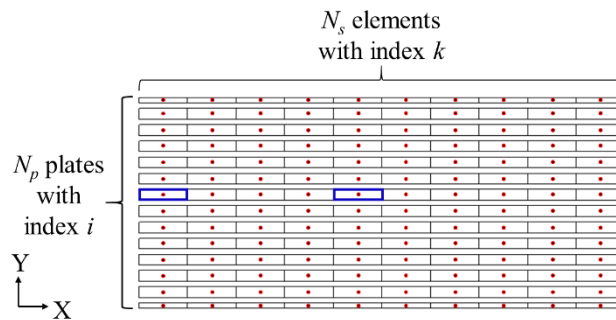
166

167 The electromagnet produces a magnetic field around 1 tesla in the air-gap ( $90 \times 50 \times 21$   
 168  $\text{mm}^3$ ). The magnetic field in the gadolinium plates is numerically simulated using a magneto-  
 169 static formulation.

170 The temperature distribution in the magnetocaloric material of the AMR involves the  
 171 corresponding  $B(H)$  local distribution. Therefore, the magnetic state of the gadolinium plates  
 172 inserted in the air-gap is numerically simulated and different “sensors” (calculation points) are  
 173 numerically placed inside the plates, in order to display the evaluated local flux density.

174 As shown in Fig. 4, the discretization considers the number  $N_p$  of indexed  $i$  rectangular  
 175 parallel plates, which are divided into  $N_s$  of indexed  $k$  equal elements, leading to  $N_s N_p$  elements  
 176 called  $e_{i,k}$  with  $i \in [1, N_p]$  and  $k \in [1, N_s]$ . The discretization resolution of the regenerator can  
 177 thus be easily increased if higher precision is required.

178



179

180

FIG. 4: *Discretization of the gadolinium regenerator in XY plane*

181

## 182 **3.2. FEM model**

183

184 The internal magnetic flux density  $B$  and internal magnetic field  $H$  of each segment is  
185 calculated for electrical coil currents ranging from 0 to 50 A with 5 A steps. The results obtained  
186 with a 3D FEM using Flux© magnetostatic solver can be considered as a reference, since this  
187 computation code can take complex magnetic phenomena into account, such as 3D effects, non-  
188 linear  $B(H)$  behavior, magnetic flux losses, demagnetization, etc. In particular, the demagnet-  
189 izing field has a strong influence on the internal magnetic field, on the magnetic flux density  
190 and on the magnetization inside the AMR.<sup>5</sup> Therefore, oversimplified hypothesis on demagnet-  
191 izing factors should be avoided when calculating the internal magnetic field in AMR materials.

192 FEM models lead to a very precise magnetic analysis but are highly time-consuming  
193 (about five minutes for each magnetostatic resolution point of our experimental prototype with  
194 a 2.80 GHz dual-core PC). Even if the FEM model is accurate, the computation cost seems to  
195 be prohibitive when this model is coupled to a multiphysics simulation loop. In this case indeed,  
196 a huge number of successive estimation points are required to insure convergence, leading to a  
197 very large computation time. The numerical results of FEM calculations are exhibited below  
198 and compared to those obtained with our semi-analytical model in section 4.

199

## 200 **3.3. Semi-analytical model based on reluctance network**

201

202 In the present work, a semi-analytical model has been designed to accurately model the  
203 distribution of the internal magnetic field at each point of the regenerator for each time step  
204 during the AMR cycle, allowing much faster calculation than FEM with comparable precision,  
205 while accounting for the heterogeneous distribution of the magnetic field in the AMR.

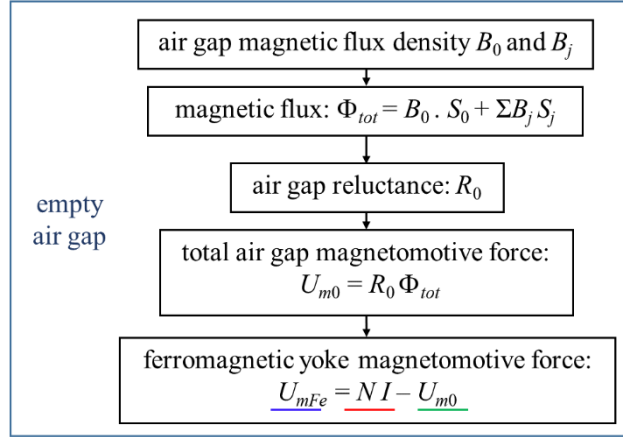
### 206 ***3.3.1. Mapping the non-linear behavior of the external ferromagnetic yoke***

207

208 The first feature of our semi-analytical model is to take into account the non-linear be-  
209 havior of the external ferromagnetic yoke of the test bench, by means of experimental measures

210 of the magnetic flux density in the empty air-gap. The calculation scheme is displayed in Fig.  
 211 5.

212



213

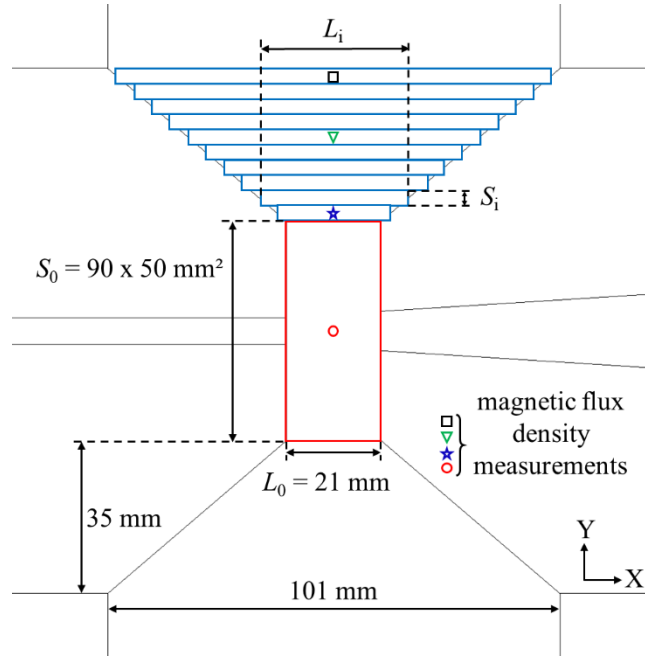
214 FIG. 5: Calculation scheme of mmf for the external ferromagnetic yoke with empty air-gap

215

216 During this step, the magnetomotive force (mmf) of the ferromagnetic circuit  $U_{mFe}$  is cal-  
 217 culated. The magnetic flux density of the central air gap  $B_0$  is precisely measured in the core of  
 218 the empty air-gap with a gauss-meter (as shown in 0), for currents ranging from 0 to 55 A with  
 219 a 5 A step. This leads to the magnetic flux in the central air gap  $\Phi_0$  [Wb] depending on the  
 220 magnetic flux density and the associated air-gap section  $S_0 = 90 \times 50 \text{ mm}^2$  (red part in Fig. 6  
 221 and Fig. 7):

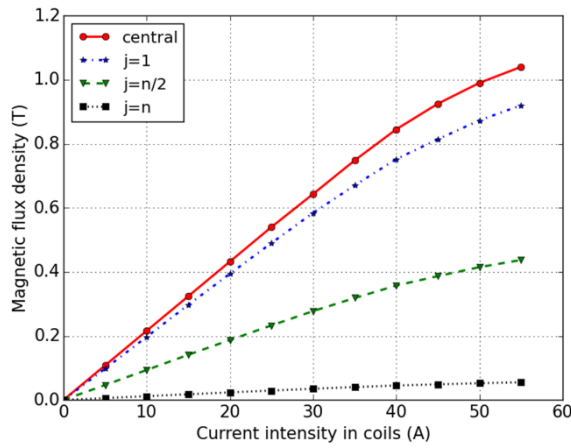
$$\Phi_0 = B_0 S_0. \quad (1)$$

222



223

FIG. 6: Air gap aspect



224

225

FIG. 7: Experimental magnetic flux density measurements

226

227 From there, the reluctance of the whole air-gap (2) is calculated considering the leakage  
 228 flux between magnetic poles outside the central rectangular air-gap (external trapezoidal air  
 229 gaps):

$$R_0 = \left( \frac{\mu_0 S_0}{L_0} + 2 \sum_{j=1}^n \frac{\mu_0 S_j}{L_j} \right)^{-1}, \quad (2)$$

230 where  $L_j$  and  $S_j$  are the length and section of the  $j^{th}$  among  $n = 50$  subdivisions of the symmetric  
 231 trapezoidal leakage flux zone (an example of segmentation with  $n = 10$  is presented in blue in

232 Fig. 6). The magnetic flux density  $B_j$  in the external trapezoidal air gap was measured and  
 233 linearly estimated along the  $n = 50$  subdivisions (the values for  $j = 1, n/2, n$  are displayed in Fig.  
 234 7). The magnetic flux in the whole empty air gap  $\Phi_{tot}$  [Wb] expresses then as:

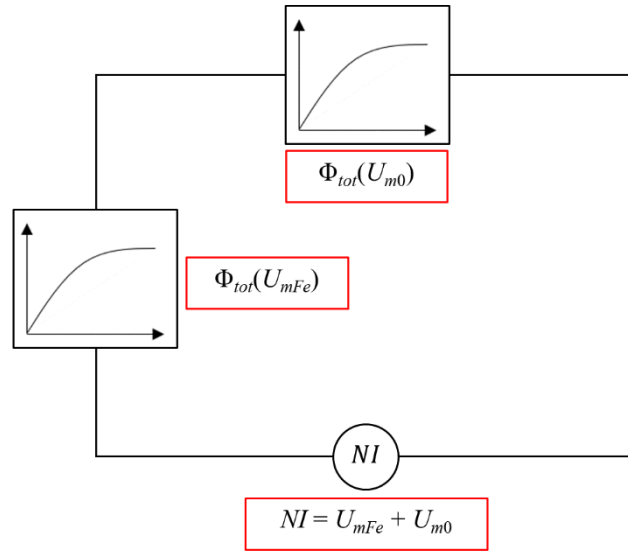
$$\Phi_{tot} = B_0 S_0 + 2 \sum_{j=1}^n B_j S_j . \quad (3)$$

235 In these conditions, the mmf values  $U_{m0}$  (equation 4) of the empty air gap are obtained  
 236 using this experimental method and compared with those calculated by the FEM, leading to a  
 237 relative difference smaller than 0.4%:

$$U_{m0} = R_0 \Phi_{tot} . \quad (4)$$

238 An equivalent diagram of the magnetic circuit with an empty air gap is displayed in Fig.  
 239 8 showing the relation between the global magnetomotive force equal to  $NI$ , the magnetomotive  
 240 force of the ferromagnetic circuit and the magnetomotive force of the empty air gap.

241



242

243 FIG. 8: Equivalent diagram for the calculation of the ferromagnetic circuit mmf

244

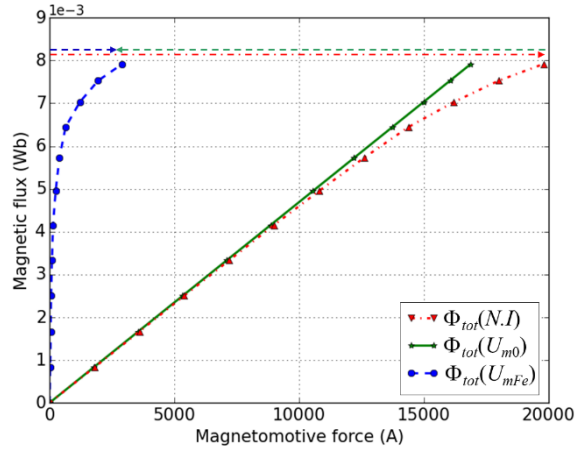
245 Therefore, the magnetomotive force  $U_{mFe}$  across the ferromagnetic circuit can be deduced  
 246 from the equivalent Kirchhoff voltage law for magnetic circuit (5), where  $I$  is the intensity of  
 247 the electric current flowing in the coils and  $N$  is the number of coil turns (Fig. 9).

$$U_{mFe} = NI - U_{m0} = NI - R_0 \Phi_{tot} . \quad (5)$$

248  $U_{mFe}$  dependence on  $\Phi_{tot}$  is obtained by evaluating (5) for an experimental dataset of currents.

249 Interpolation can map  $\Phi_{tot}(U_{mFe})$  and  $U_{mFe}(\Phi_{tot})$  dependences.

250



251

252 FIG. 9: Obtaining the magnetomotive force of the ferromagnetic circuit

253

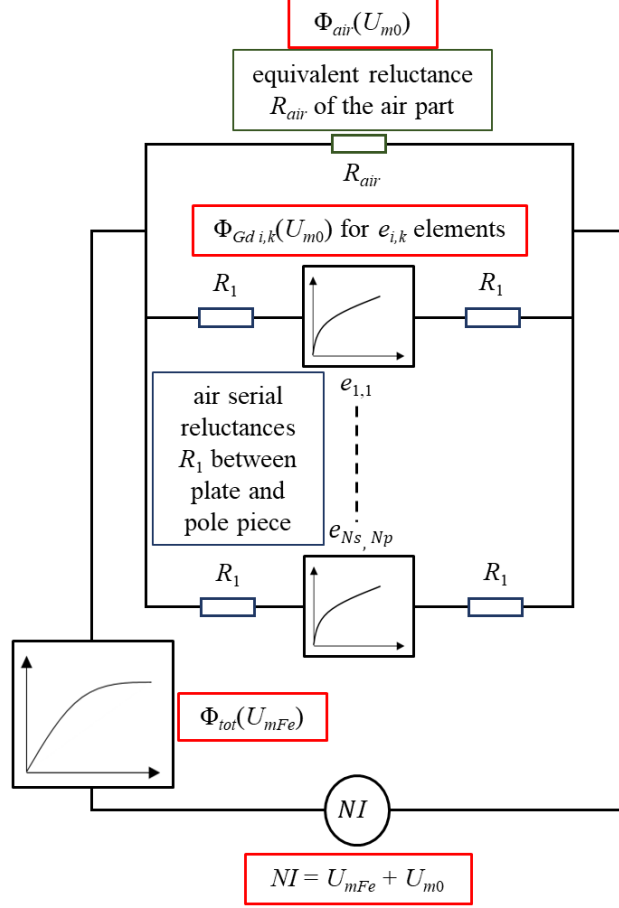
### 254 3.3.2. Computing magnetic flux distribution in the AMR regenerator

255

256 In the second step, we analyse the magnetic flux distribution in the AMR regenerator  
257 plates for an inhomogeneous temperature distribution. The magnetic flux density distribution  
258  $B_{i,k}$  for each element  $e_{i,k}$  is computed in the discretized regenerator, for a given coil current at a  
259 given temperature distribution  $T_{i,k}$  in the regenerator. This step considers the magnetic behavior  
260 of the ferromagnetic yoke  $U_{mFe}(\Phi_{tot})$  obtained previously and represented in Fig. 9.

261 Fig. 10 displays the magnetic equivalent diagram of the air-gap with gadolinium plates.

262



263

264

FIG. 10: *Magnetic equivalent diagram of the air-gap with gadolinium plates*

265

266

267

268

269

270

271

272

273

274

275

276

The parallel-series circuit, supplied with the coil's mmf ( $NI$ ) involves the non-linear behavior  $U_{mFe}(\Phi_{tot})$  of external ferromagnetic yoke, the non-linear dependence  $\Phi_{i,k}(U_{mGd\ i,k})$  of each discretization element  $e_{i,k}$  of the regenerator and the reluctances of air regions. We can observe two kinds of air regions: a region in the air gap, corresponding to the external magnetic flux  $\Phi_{Air}$  through the  $R_{air}$  reluctance, and a set of  $N_p N_s$  regions located on the path of the magnetic flux through each element  $e_{i,k}$  of the regenerator of  $R_1$  reluctance. Each element  $e_{i,k}$  is bounded by two  $R_1$  reluctances in series with its non-linear  $U_{mGd\ i,k}(\Phi_{i,k})$  (as shown in Fig. 11).

Since the temperature  $T_{i,k}$  of each element  $e_{i,k}$  is known, the curve  $B_{i,k}(H_{i,k})$  is determined by the approximation of the experimental MCM characteristic curves  $B(H, T)$  for  $T = T_{i,k}$ . This allows to calculate the spatial distribution of the characteristic  $U_{mGd\ i,k}(\Phi_{i,k})$ , using (6) and (7), where  $S_{i,k}$  is the element section and  $l$  the width of the element:

$$\Phi_{i,k} = B_{i,k}(H_{i,k}, T_{i,k}) S_{i,k}, \quad (6)$$

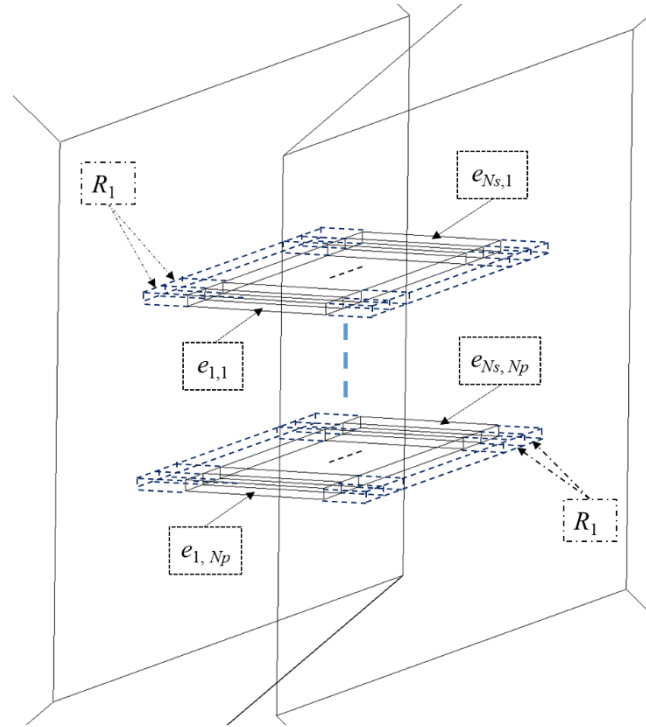
$$U_{mGd\,i,k} = \int H_{i,k} \, dl = H_{i,k} \, l. \quad (7)$$

277

278 The mmf  $U_{mGd\,i,k}$  of each element in series with two  $R_1$  reluctances leads to the global  
 279 mmf  $U_{m0}$  in the air gap, as a function of the flux  $\Phi_{i,k}$  through the element  $e_{i,k}$  :

$$U_{m0} = U_{mGd\,i,k} + 2\Phi_{i,k} R_1. \quad (8)$$

280



281

FIG. 11: 3D view of the air-gap with some gadolinium plates

282

283

284 In order to identify the magnetic flux distribution in the air spacing of the air-gap, it is  
 285 necessary to compute the reluctance  $R_{air}$  with (9):

$$\frac{1}{R_{air}} = \frac{1}{R_0} - \sum_{k=1}^{N_p} \frac{1}{R_k} \quad \text{with} \quad R_k = \frac{L_0}{\mu_0 S_k}, \quad (9)$$

286 where  $R_k$  is the reluctance of the parallelepipedic air space crossed by the magnetic flux flowing  
 287 through the cross-section  $S_k$  of the gadolinium  $k$  plate.

288

289 The magnetic flux of the air spacing inside the air-gap is calculated by (10), considering  
 290 the linear dependence of the magnetic flux in the air gap:

$$\Phi_{air} = \frac{U_{m0}}{R_{air}}. \quad (10)$$

291 This leads to the mapping function  $\Phi_{tot}(U_{m0})$  of the global air gap flux noted  $\Phi_{tot}$  function of the  
 292 total mmf of the gap including the regenerator ( $U_{m0}$ ). For a given magnetomotive force  $U_{m0}$ , the  
 293 global magnetic flux is obtained by adding all element fluxes  $\Phi_{i,k}$  with the magnetic flux  $\Phi_{air}$   
 294 in the air gap (11):

$$\Phi_{tot}(U_{m0}) = \sum_{k=1}^{Np} \sum_{i=1}^{Ns} \Phi_{i,k}(U_{m0}) + \Phi_{air}(U_{m0}). \quad (11)$$

295 What remains to be done is to compute the cartography  $\Theta(\Phi_{tot})$  of the total magnetomo-  
 296 tive force corresponding to a total magnetic flux, by adding the magnetomotive force in the  
 297 global air gap, using the inverse interpolation of  $\Phi_{tot}(U_{m0})$  obtained with (11). Thus,  $(N.I)$  is  
 298 obtained by interpolation of  $\Theta$  for a regular dataset of the magnetic flux between 0 and a max-  
 299 imum value, according to Kirchhoff's law for magnetic circuit (12):

$$\Theta = NI = U_{mFe}(\Phi_{tot}) + U_{m0}(\Phi_{tot}). \quad (12)$$

300 The proposed algorithm contains several sub-functions considering the nonlinearities in  
 301 active magnetic materials (gadolinium plates, ferromagnetic yoke). In Table. I, we observe the  
 302 complete scheme of the algorithm. The different steps are exposed in detail below, and two  
 303 preliminary computations are necessary:

- 304 - external ferromagnetic circuit behavior  $\Phi_{tot}(U_{mFe})$
- 305 -  $R_{air}$  and  $R_1$  air reluctances

① Inputs: $T_{i,k}, I$
② Mapping $\Phi_{i,k}(U_{m0})$ , equations (6) to (8) a) Obtaining magnetic behavior interpolation functions $B(H)_{i,k}$ for each element $e_{i,k}$ . b) Transforming $B(H)_{i,k}$ into a flux mmf interpolation function $\Phi_{i,k}(U_{mGd,i,k})$ – Eq (6) and (7) c) Transforming $U_{mGd}$ variable in $U_{m0}$ – Eq (8)
③ Considering the linear dependence of the magnetic flux $\Phi_{air}(U_{m0})$ in the air gap – Eq (10)
④ Mapping function of the global air gap flux $\Phi_{tot}(U_{m0})$ – Eq (11)
⑤ Computing the cartography $\Theta(\Phi)$ – Eq (12)
⑥ Computing the total mmf $\Phi_{tot}$ for a given current $I$

⑦ Obtaining the gap mmf $U_{m0}$ by interpolation of $\Phi_{tot}(U_{m0})$
⑧ Obtaining the magnetic flux $\Phi_{i,k}$ through each element by interpolation of $\Phi_{i,k}(U_{m0})$
⑨ Obtaining the mmf $U_{mGd\ i,k}$ of each element with the dependence $\Phi_{i,k}(U_{mGd\ i,k})$
⑩ Obtaining the internal magnetic flux density $B_{i,k}$ and internal magnetic field $H_{i,k}$ of each element

306 TABLE. I: Complete scheme of the air-gap with gadolinium plates and equivalences

307

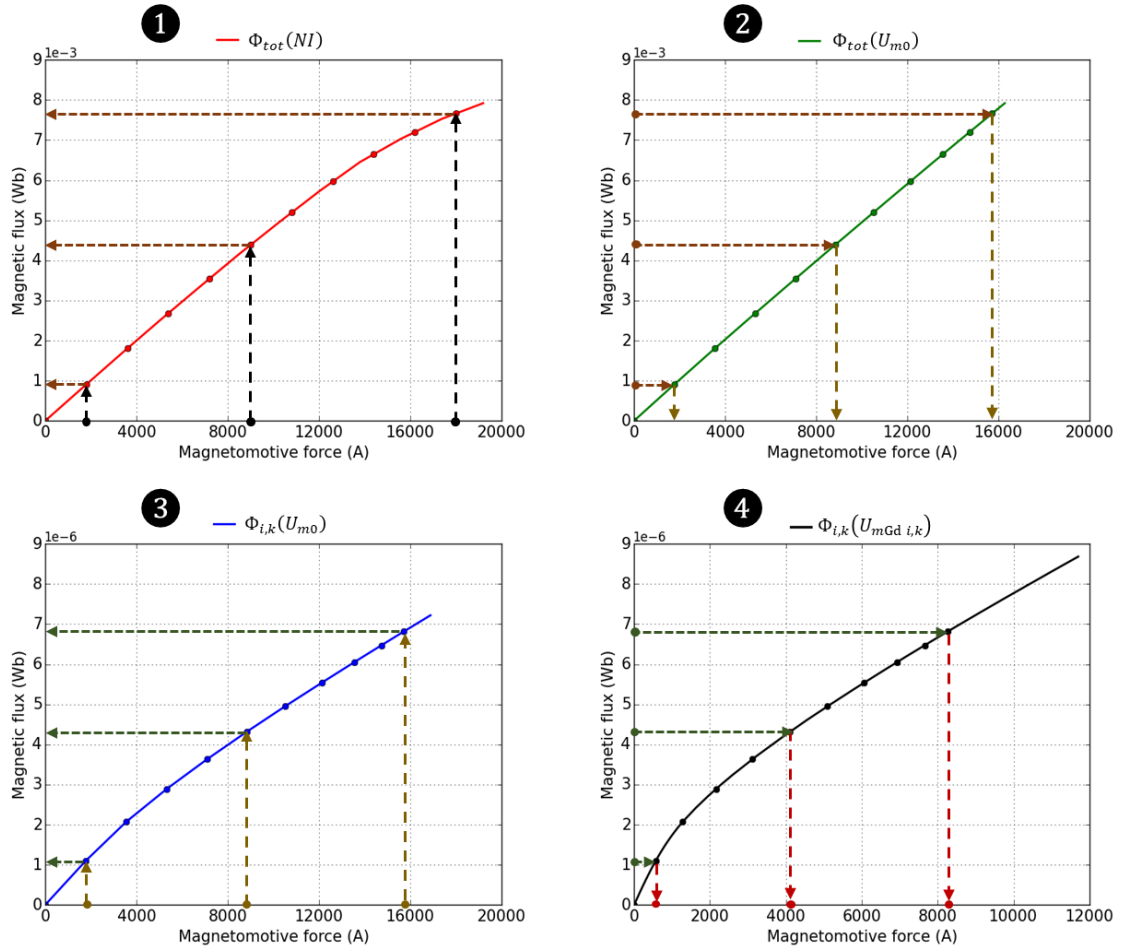
### 308 3.3.3. Graphical interpretation of the algorithm

309

310 Thereafter, in these conditions, a series of interpolations have to be performed in order to  
 311 obtain the internal  $B_{i,k}$  and  $H_{i,k}$  values of each element of the magnetocaloric material:

- 312 - the global magnetic flux through the gap  $\Phi_{tot}$  is calculated from the current  $I$  in the coils  
 313 (consequently  $NI$ ) and the mapping  $\Phi_{tot}(NI)$ . Thus, the first curve fit method can be per-  
 314 formed (step ⑥ in Table. I and interpolation ① in Fig. 12);
- 315 - the second interpolation is performed to obtain the mmf of the gap  $U_{m0}$ , which depends  
 316 on the curve  $\Phi_{tot}(U_{m0})$ , using the values of the magnetic flux in the gap obtained with the  
 317 previous interpolation (step ⑦ in Table. I and interpolation ② in Fig. 12);
- 318 - the next interpolation aims at obtaining the magnetic flux in each segment using the mmf  
 319 calculated previously. For this purpose, it is necessary to use the curve connecting the  
 320 magnetic flux of the segment and the mmf of the gap since the dependence  $\Phi_{i,k}(U_{m0})$  is  
 321 known for each element  $e_{i,k}$  (step ⑧ in Table. I and interpolation ③ in Fig. 12);
- 322 - the last curve fit method is achieved to obtain the mmf of each element, which depends  
 323 on the curve  $\Phi_{i,k}(U_{mGd\ i,k})$ , using the values of the magnetic flux of the corresponding  
 324 segment obtained with the previous interpolation (step ⑨ in Table. I and interpolation  
 325 ④ in Fig. 12).

326



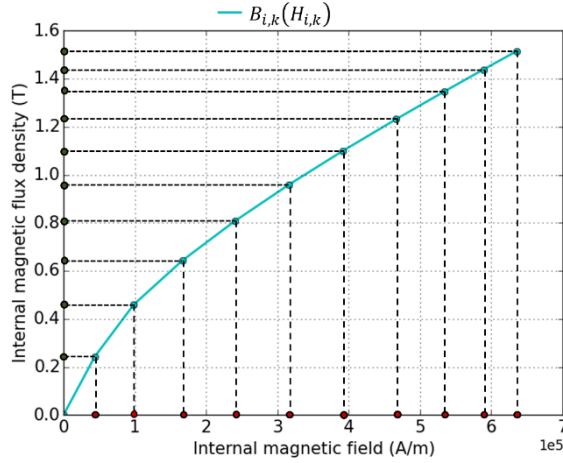
327

328 FIG. 12: Successive interpolations for obtaining the magnetic flux and the magnetomotive force in  
 329 each segment

330

331 The ultimate step is to get the internal magnetic flux density  $B_{i,k}$  and internal magnetic  
 332 field  $H_{i,k}$  of each element, by dividing  $\Phi_{i,k}$  and  $U_{mGd i,k}$  respectively by the section  $S_{i,k}$  and the  
 333 length  $l$  (see example in Fig. 13). So, the characteristics  $B_{i,k}(H_{i,k})$  of the magnetocaloric material  
 334 (gadolinium in our case) are obtained after achievement of all the steps with our code developed  
 335 in Python language.

336



337

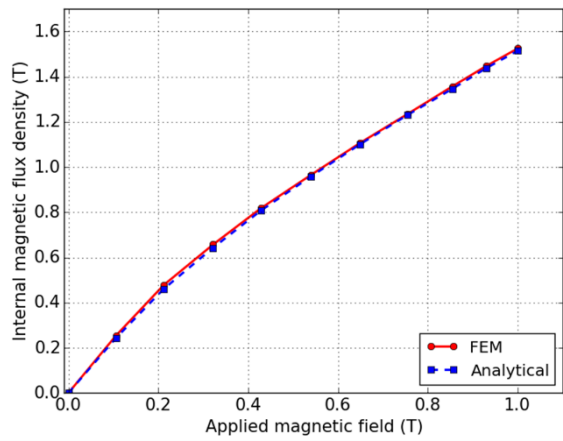
338 FIG. 13: Obtaining the internal magnetic flux density and magnetic field of an element  $e_{i,k}$

339 **4. Results and comparisons**

340

341 The results obtained by the FEM (Flux3D©) for the magnetic flux density calculation in  
 342 a ten-fold segmented plate of gadolinium at imposed uniform temperature  $T = 293$  K are com-  
 343 pared to the results of our semi-analytical model. The outputs for the central and the external  
 344 elements of the central plate are presented in Fig. 14 and Fig. 15, respectively (the correspond-  
 345 ing segments are highlighted in blue in Fig. 4). The maximum difference between these results  
 346 is lower than 2%.

347



348

349 FIG. 14: Magnetic curve of the central element (central gadolinium plate)

350

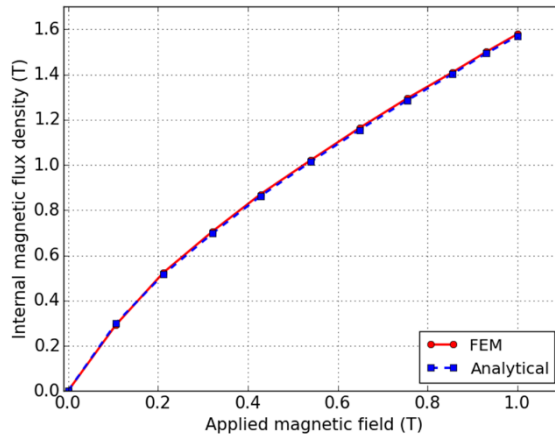


FIG. 15: *Magnetic curve of the external element (central gadolinium plate)*

351

352

353

354

355

356

357

358

359

The difference between the magnetic flux density curves of the two elements shows how much the magnetic flux density is depending on the position of the element inside the air gap, even if the temperature is uniform. Indeed, the external lines of the magnetic flux density concentrate at the ends of the regenerator plates, so that the magnetic flux density is higher (0.05 T) at the ends than at the center of the plates.

360

361

362

363

364

365

366

367

368

369

More thoroughly, it has been shown in Ref. 13 that strong inhomogeneities in the magnetic field inside an empty air gap are induced when introducing a magnetocaloric plate into an applied magnetic field, leading to a higher magnetic field intensity in the air, along with a large drop of the latter inside the plate very close to the ends. This is due to both the magnetic permeability of gadolinium ( $\mu_r \sim 1.5$ ) and the demagnetizing field on the boundary surfaces, which increases the axial demagnetization factor close to the ends of the regenerator plate. Since the magnetic flux is conservative, the decrease of the magnetic field intensity at each end of the magnetocaloric plate leads to a shift of the magnetic curve toward lower values of  $H$ , as shown in Fig. 15.

370

371

372

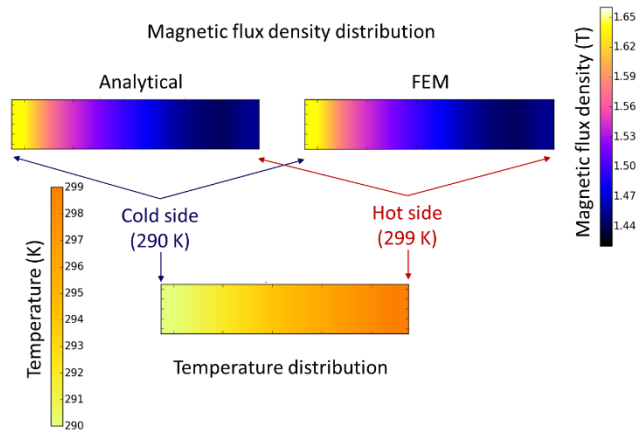
373

374

Moreover, both the magnetic flux density and the magnetic field depend strongly on temperature, more particularly around the Curie temperature ( $T_c \approx 293$  K for gadolinium). The comparison will further focus on the magnetic flux distribution in the central gadolinium plate, with imposed temperatures at each end (left cold side 290 K; right hot side 299 K). For this purpose, Fig. 16 shows the magnetic flux density distributions in the central gadolinium plate

375 that have been obtained by the FEM and semi-analytical models respectively, with 50 A current  
 376 intensity in the coils producing 1 T magnetic flux density in the empty air gap.

377



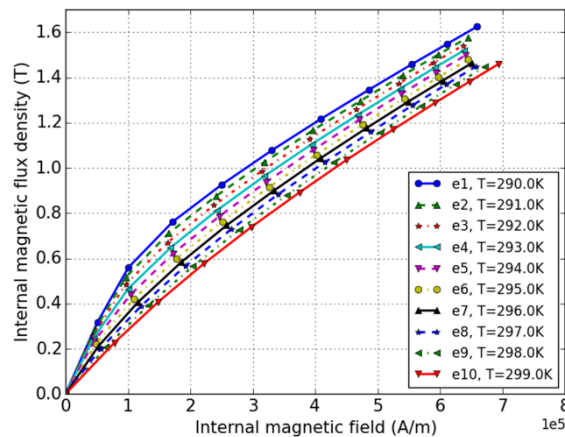
378

379 FIG. 16: *Magnetic flux density distribution comparison*

380

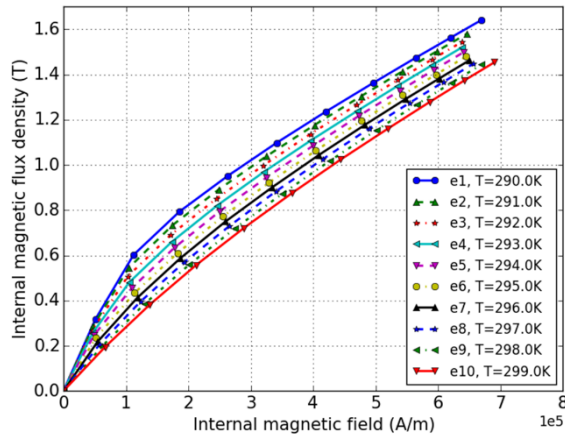
381 The accuracy of the semi-analytical model can be highlighted in the case of a linear tem-  
 382 perature gradient from 290K to 299K imposed between the cold and the hot sides of the regen-  
 383 erator. The dependency of the internal magnetic flux density on the internal magnetic field in  
 384 the gadolinium central plate divided into 10 equal elements is calculated with our semi-analyt-  
 385 ical model and with Flux3D<sup>®</sup> and displayed on Fig. 17 and Fig. 18, respectively.

386



387

388 FIG. 17: *B(H) curves at each point of the regenerator at corresponding temperature (semi-analytical)*



389

390 FIG. 18:  $B(H)$  curves at each point of the regenerator at corresponding temperature (FEM)

391

392 As can be seen in both figures, the magnetic flux density is much higher at the cold side  
 393 of the plate, because of a higher magnetization due to the ferromagnetic state of the gadolinium  
 394 under its Curie temperature, while being much lower at the hot side above the Curie temperature  
 395 (paramagnetic state).

396 No significant difference can be detected between the two figures, which confirms the  
 397 good accuracy of our semi-analytical model. No discrepancy higher than 3% was obtained be-  
 398 tween these two simulations.

399

400 As a final comparison, the two different methods for obtaining internal magnetic field  
 401 and magnetic flux density of the magnetocaloric material exhibit the following advantages and  
 402 drawbacks:

- 403 - the finite element method (FEM) leads to very precise magnetic analysis (3D phenomena)
- 404 but is highly time-consuming when using a fine spatial resolution grid. For instance, the
- 405 calculation time needed for achieving the FEM numerical simulation applied to the evolution
- 406 of internal magnetic field and magnetic flux density in the whole magnetic system with a 5A
- 407 step [0 : 50, 5A] is around 35 min with a 2.80 GHz dual-core PC;
- 408 - the semi-analytical model always requires much less time than the FEM resolution and offers
- 409 good analysis precision with very similar results. The calculation time needed for the same
- 410 analysis under same conditions drops to around 5 s with the same computer.

411

## 412 5. Conclusions

413

414 A semi-analytical model based on a reluctance network is proposed to calculate the inter-  
415 nal magnetic field  $H$  and internal magnetic flux density  $B$  when introducing a magnetocaloric  
416 stack of parallel plates into a magnetic air gap. The computation time needed with our model  
417 for obtaining internal magnetic field  $H$  and magnetic flux density  $B$  at each point of the whole  
418 magnetic system is around four hundred time shorter, compared to a complete FEM solver  
419 resolution for the same system in the same conditions.

420 The semi-analytical model is directly applicable and can easily be extended to rotary  
421 magnetocaloric devices. A multiphysics analysis will be described in a further paper, in which  
422 the presented magnetostatic model is combined with a thermo-fluidic model, allowing to  
423 achieve the simulation of 5 AMR cycles applied to the whole system within only 5 minutes,  
424 instead of 4 hours with 3D FEM<sup>12</sup> (using a 2.80 GHz dual-core PC). Besides, the magnetic  
425 results obtained with our semi-analytical model are very close to those of the FEM solver  
426 Flux3D<sup>®</sup>, which proves the efficiency of our model.

427 Moreover, our semi-analytical model was applied efficiently to an optimization process  
428 of an AMR refrigeration system. The model involves the multi-physics phenomena occurring  
429 during the magnetic refrigeration process and simulates both the magnetocaloric material be-  
430 havior, the instantaneous heat exchanges and the evolution of the whole magnetocaloric system  
431 undergoing successive AMR cycles with a controlled periodic applied magnetic field. This al-  
432 lows to simulate the experimental behavior of our magnetocaloric test bench developed at the  
433 FEMTO-ST Institute.

434 More generally, our analytical reluctance-based model could easily be adapted to any  
435 other magnetocaloric regenerator device to save huge calculation time without losing precision  
436 and to allow easier multi-parametric optimization.

437

438

439

440 **References**

- 441 <sup>1</sup> K.A. Gschneider, V.K. Pecharsky, Magnetocaloric materials, *Ann. Rev. Mater. Sc.* 30(1) (2000) 387–  
442 429.
- 443 <sup>2</sup> W. Steyert, Magnetic refrigerators for use at room temperature and below, *Journal de Physique Col-*  
444 *loques* 39 (1978) C6-1598-C6-1604.
- 445 <sup>3</sup> C. Espanet, C. Kieffer, A. Mira, S. Giurgea, F. Gustin, Optimal design of a special permanent magnet  
446 synchronous machine for magnetocaloric refrigeration, *Energy Conversion Congress and Exposition*,  
447 5019–5025, Denver, 2013
- 448 <sup>4</sup> W. Dai et al., Application of high-energy Nd-Fe-B magnets in the magnetic refrigeration, *J. Magn.*  
449 *Magn. Mat.* 218 (2000) 25-30.
- 450 <sup>5</sup> D. Vuarnoz T. Kawanami, Experimental validation of a coupled magneto-thermal model for a flat-  
451 parallel-plate active magnetic regenerator, *Appl. Therm. Eng.* 54 (2013) 433-439.
- 452 <sup>6</sup> A. Kitnovski, U. Plaznik, U. Tomc, A. Poderoš, Present and future caloric refrigeration and heat-pump  
453 technologies, *Int. J. Refrig.* 57 (2015) 288-298.
- 454 <sup>7</sup> C. Espanet, C. Kieffer, A. Mira, S. Giurgea, F. Gustin, Optimal design of a special permanent magnet  
455 synchronous machine for magnetocaloric refrigeration, *Energy Conversion Congress and Exposition*,  
456 Denver, 2013, pp 5019–5025.
- 457 <sup>8</sup> A. Mira, C. Espanet, T. de Larochelambert, S. Giurgea, P. Nika, Multi-physics analysis of a magneto-  
458 caloric cooling system, *Compumag* (2013), 44.
- 459 <sup>9</sup> M.G. Schroeder, E. Brehob, A flexible numerical model of a multistage active magnetocaloric regen-  
460 erator, *Int. J. Refrig.* 65 (2016) 250-257.
- 461 <sup>10</sup>C. Aprea, A. Maiorino, A flexible numerical model to study an active magnetic refrigerator for near  
462 room temperature applications, *Applied Energy* 87 (2010) 2690-2698.
- 463 <sup>11</sup>B. Torregrosa-Jaime, J.M. Corberán, J. Payá, K. Engelbrecht, An efficient numerical scheme for the  
464 simulation of parallel-plate active magnetic regenerators, *Int. J. Refrig.* 58 (2015) 121-130.
- 465 <sup>12</sup>A. Mira, C. Espanet, T. de Larochelambert, S. Giurgea, P. Nika, Influence of computing magnetic field  
466 on thermal performance of a magnetocaloric cooling system, *Eur. J. Electr. Eng.* 17/3-4 (2014) 151-  
467 170.
- 468 <sup>13</sup>A. Mira, T. de Larochelambert, C. Espanet, S. Giurgea, P. Nika, C.R.H. Bahl, R. Bjørk, K.K. Nielsen,  
469 Influence of magnetization on applied magnetic field in various AMR regenerators, *J. Appl. Phys.*122,  
470 133901 (2017).

471 <sup>14</sup>A. Plait, S. Giurgea, C. Espanet, T de Laroche Lambert, P. Nika, Magnetocaloric bench: analytical  
472 model for gadolinium characteristics, Seventh IIF-IIR Int. Conf. Magn. Refrig. Room Temp., (2016).